Electronic Supplementary Material (ESI) for Dalton Transactions.
This journal is © The Royal Society of Chemistry 2016

SUPPORTING INFORMATION

Synergistic photomagnetic effects in coordination polymer heterostructure particles of Hofmann-like Fe(4-phenylpyridine)2[Ni(CN)4]·0.5H2O and K0.4Ni[Cr(CN)6]0.8·nH2O

Corey R. Gros,[a] Marcus K. Peprah,[b] Ashley C. Felts,[a] Tatiana V. Brinzari,[b] Olivia N. Risset,[a] John M. Cain,[a] Cauê F. Ferreira,[a] Mark W. Meisel,[b*] Daniel R. Talham[a*]

[a]Department of Chemistry, University of Florida, Gainesville, FL 32611-7200
[b]Department of Physics and National High Magnetic Field Laboratory, University of Florida, Gainesville, FL 32611-8440

Table SI-1. Warming and cooling rates for magnetometry studies. Note: when the data are being acquired, the sample is stable at a given temperature and the maximum rates for changing the temperature between set points are listed.

Sample	Cooling Rates	Warming Rates
Single phase Hofmann-like sample	2 K/min for 300 K to 100 K 5 K /min for 100 K to 5 K	1 K/min for 5 K to 100 K 5 K/min for 100 K to 150 K
Heterostructure	2 K/min for 300 K to 100 K 4 K/min for 100 K to 5 K	1 K/min for 5 K to 100 K

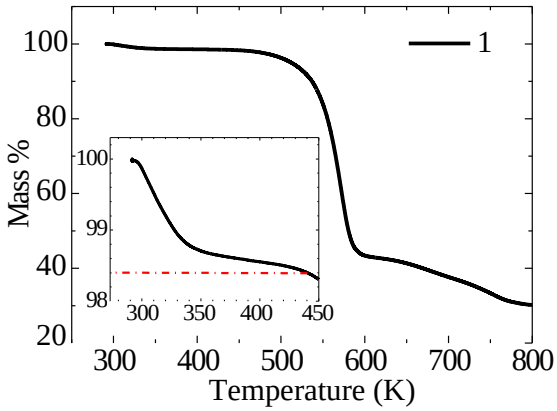

Figure SI-1. TGA analysis of compound **1**, illustrating the decomposition profile of the Hofmann seed particles as a function of temperature. The initial weight loss is approximately 1.6% attributed to guest water molecules within the Hofmann lattice, suggesting an overall chemical formula of $Fe(phpy)_2[Ni(CN)_4]\cdot 0.5H_2O$.

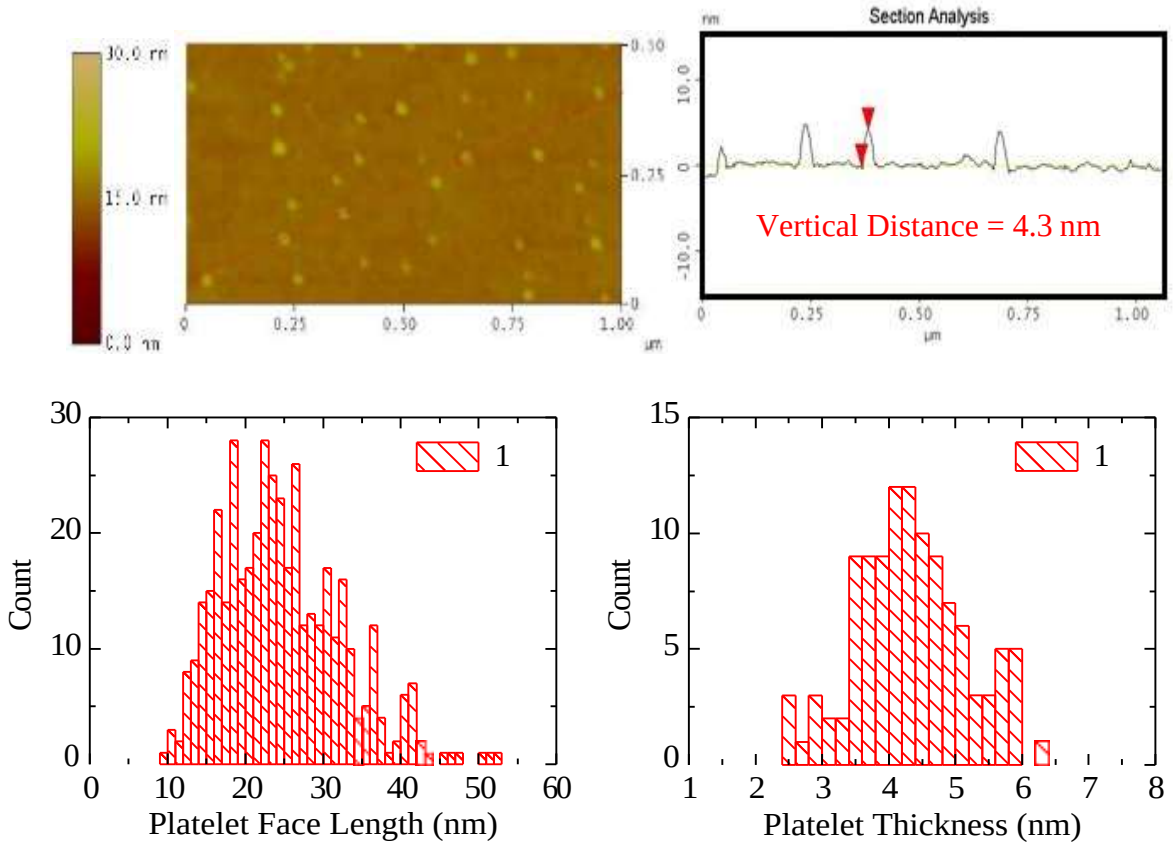

Figure SI-2. AFM image (upper left) and trace analysis (upper right) of seed Hofmann particles (**1**) dispersed on a glass surface after drop-casting from a toluene suspension. An average particle thickness of 4.3 ± 0.8 nm is determined by the mean of the vertical distances of over 100 particles. An average platelet face length of 25 ± 8 nm is determined from TEM images (Figure 2). Lower left and right panels: histograms illustrating size distributions of platelet face lengths and thicknesses (AFM).

Table SI-2. Metal ratio analysis for compounds **1** and **2** obtained by bulk Energy Dispersive X-ray Spectroscopy (EDS).

Compound	Fe (%)	Ni (%)	Cr (%)
1	47.02 ± 1.76	52.83 ± 1.65	n/a
2	25.19 ± 0.59	54.25 ± 0.26	20.56 ± 0.46

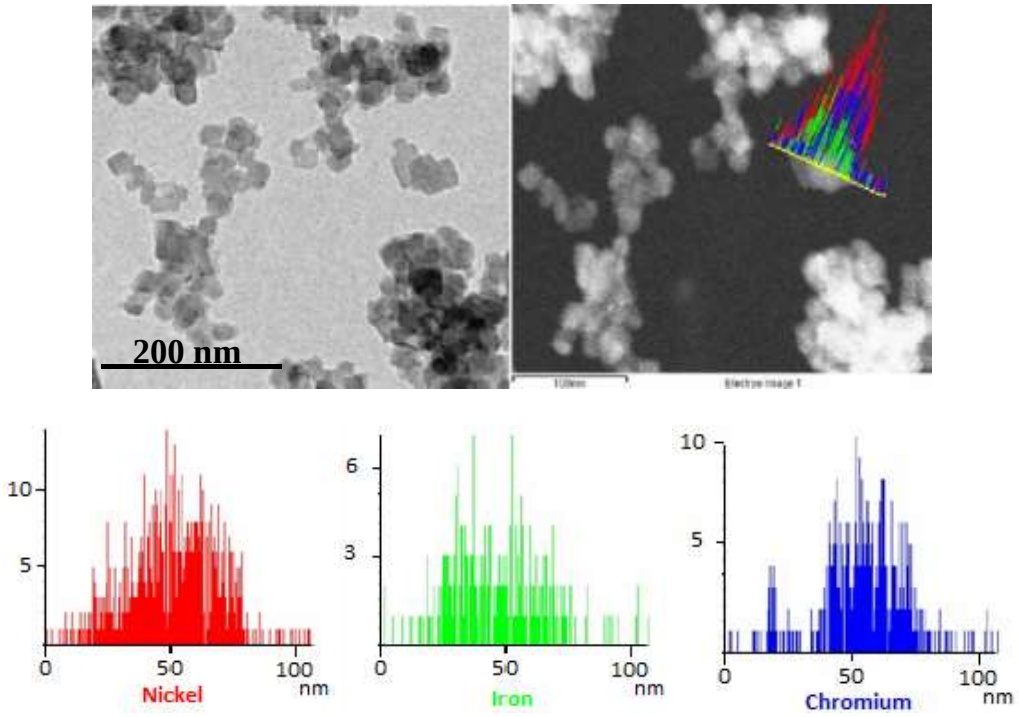

Figure SI-3. EDS linescan of heterostructure particles in **2** illustrating the presence of metals from both compounds in the heterostructure particle, supporting the heterogeneous growth of the NiCr-PBA on the Hofmann-like seed compound. Top row: TEM image and dark-field TEM image showing the region of the EDS scan. Bottom row: Counts vs distance across the scan for each metal. The data shown above are consistent with multiple scans on different areas of the sample.

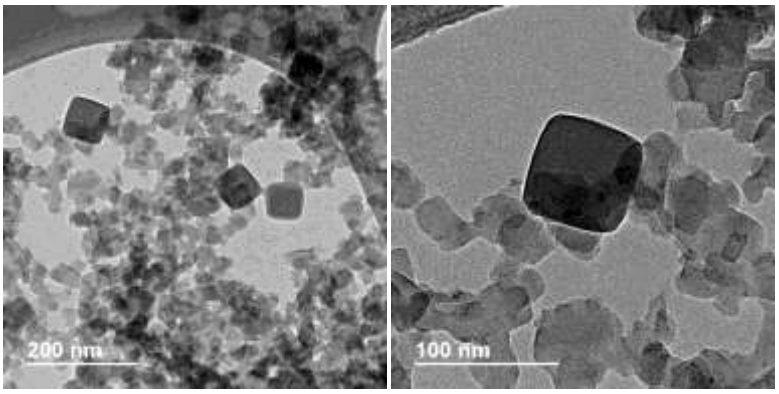

Figure SI-4. TEM images depicting homogeneous precipitation of cubic NiCr-PBA particles during a failed heterostructure synthesis. These images contrast the size and morphology of Hofmann and NiCr-PBA particles, highlighting the ease in detecting a physical mixture of the particles rather than heterogeneous growth of NiCr-PBA on the Hofmann particles during heterostructure synthesis.

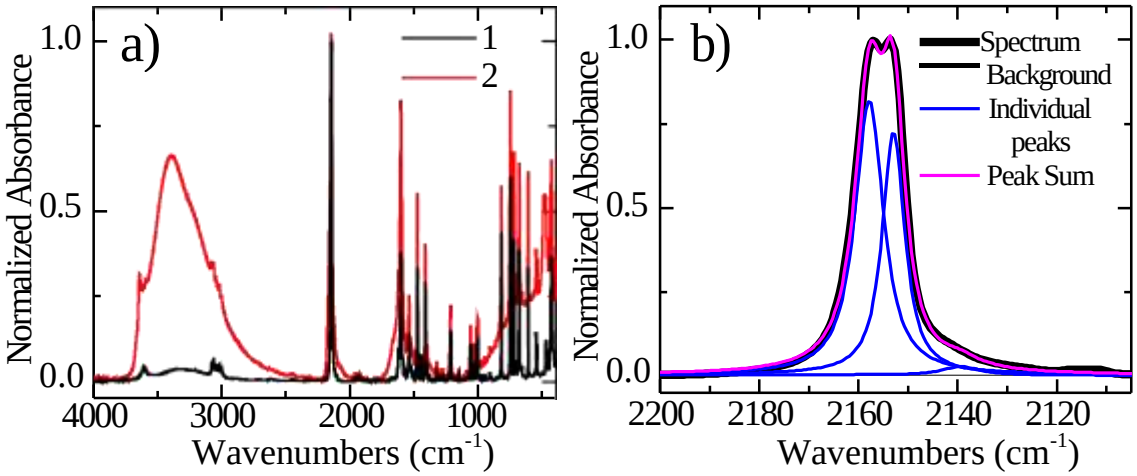

Figure SI-5. Room temperature FTIR spectra of (a) **1** and **2**, and (b) the deconvolution of the ν(CN) bands of the single-phase Hofmann compound (**1**). The fitting parameters appear in Table SI-3.

Table SI-3. Room temperature FTIR fitting parameters of the ν(CN) region for **1** and **2**, reporting relevant bridging (br) and terminal (t) stretching modes.

	1		**2**		PBA reference	
	Peak Center	FWHM (cm^{-1})	Peak Center (cm^{-1})	FWHM (cm^{-1})	Peak Center	FWHM (cm^{-1})
NiCr-PBA (t)	n/a	n/a	2132	16.9	2130[a]	------
Hofmann (br)	2139	9.4	2143	10.5	n/a	n/a
Hofmann (br)	2152	5.5	2152	8.1	n/a	n/a
Hofmann (br)	2157	6.9	2157	9.8	n/a	n/a
FeCr interface (br)	n/a	n/a	2160	18.6	2160[b]	------
NiCr-PBA (br)	n/a	n/a	2171	24.7	2174[a]	21.2[a]

[a]Data reported in reference 23. [b]Data reported in reference 49.

a)

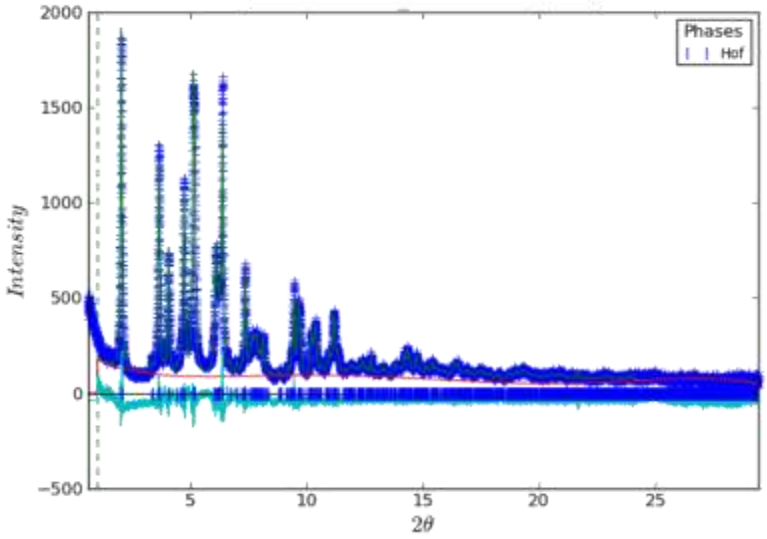

b)

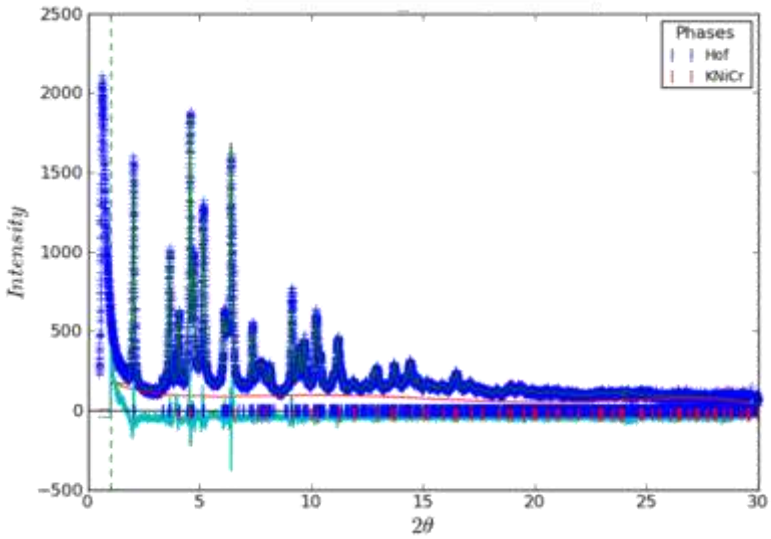

Figure SI-6. (a) Pawley fit of a PXRD pattern of **1** indexed to a monoclinic C2/m (no. 12) space group. R=5.383%, wR=10.258%, χ^2=1.39, λ = 0.414169 Å. (b) Pawley fit of a PXRD pattern of **2** using two phases, overall wR=12.302%, χ^2=1.81, λ = 0.414169 Å. The Hofmann phase is fit in the space group C2/m, R=1.218%, while the NiCr-PBA phase is fit using the space group Fm-3m, R=5.990%. Resulting unit cell parameters are reported in Table SI-4.

Table SI-4. Unit cell parameters extracted from Pawley fits of PXRD patterns of **1** and **2**.

Sample	Space Group	a (Å)	b (Å)	c (Å)	α (°)	β (°)	γ (°)
1	C2/m	24.5028(5)	7.4500(5)	6.7952(5)	90.0(5)	107.285(5)	90.0(5)
2	C2/m	24.563(5)	7.421(5)	6.821(5)	90.0(5)	107.461(5)	90.0(5)
	Fm-3m	10.380(5)	10.380(5)	10.380(5)	90.0(5)	90.0(5)	90.0(5)

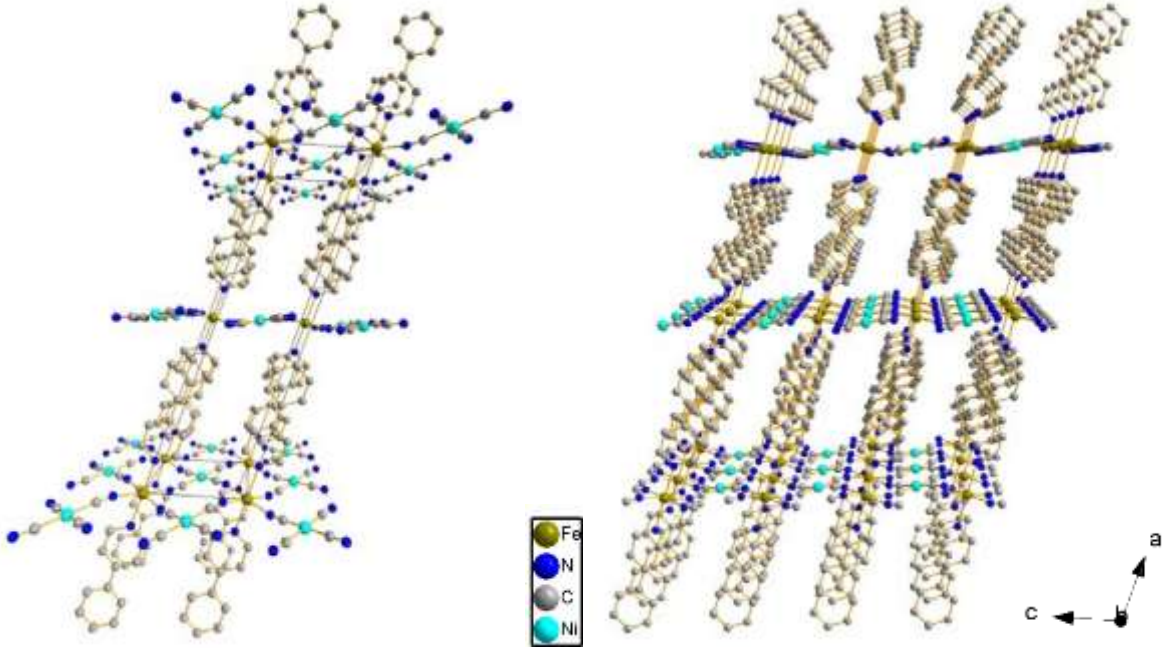

Figure SI-7. Suggested structure and extended structure of the single-phase Hofmann compound (**1**) based on PXRD pattern indexed to a monoclinic C2/m (no. 12) space group and comparison to a similar published structure.

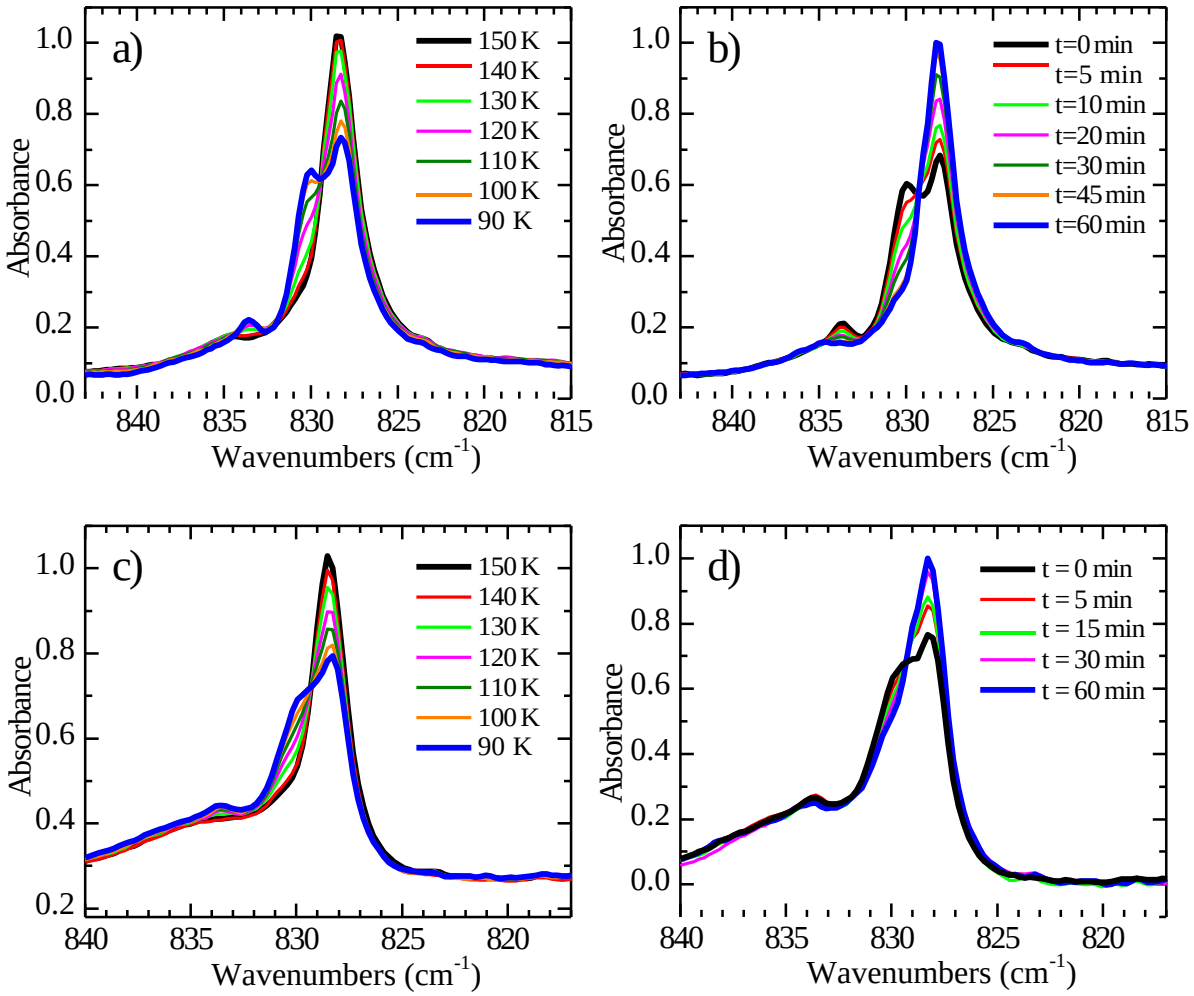

Figure SI-8. Variable-temperature FTIR data illustrating the Hofmann spin transition in single-phase and heterostructure compounds. VT-FTIR data monitor the changes in a phpy γ(CH) mode as a function of temperature and irradiation in seed compound **1** (a,b) and heterostructure **2** (c,d) as the Hofmann component undergoes thermal and photoinduced spin transitions. A partial thermal spin transition from HS (828 cm^{-1}) to LS (830 cm^{-1}) is observed upon cooling each sample, which is reversed upon irradiation at 20 K.

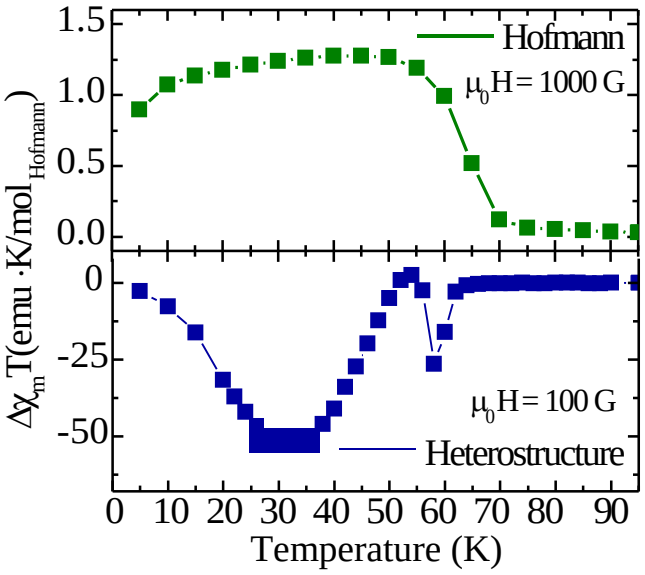

Figure SI-9. SQUID difference plot (light – dark) of **1** and **2**. Data are normalized to the amount of photoactive Hofmann component illustrating the temperature profiles of the photoinduced changes and relaxation processes. Comparison of the two data sets highlights the increased magnitude of the photoeffect in the heterostructure relative to the single-phase component alone.

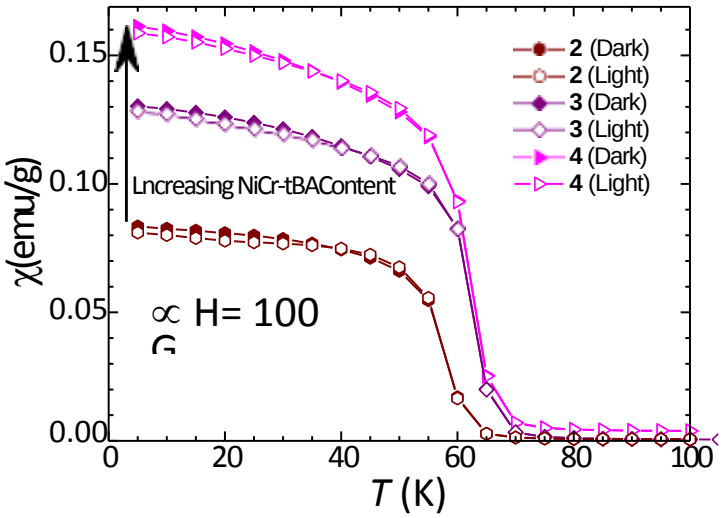

Figure SI-10. Mass susceptibility versus temperature data of heterostructure sample **2**, in addition to similar heterostructures (**3** and **4**) synthesized with higher-concentration NiCr-PBA precursors resulting in larger NiCr-PBA contents.[38] Data were field-cooled and collected at an applied field of 100 G in both the dark state (closed symbols) and the light state (open symbols), referring to pre- and post-irradiation measurements respectively. The arrow indicates the direction of increasing NiCr–PBA content. The transition temperature for sample **3** and **4** appears higher than sample **2**, suggesting that the NiCr-PBA feature size in sample **2** may be below the bulk magnetic coherence length resulting in T_c suppression.

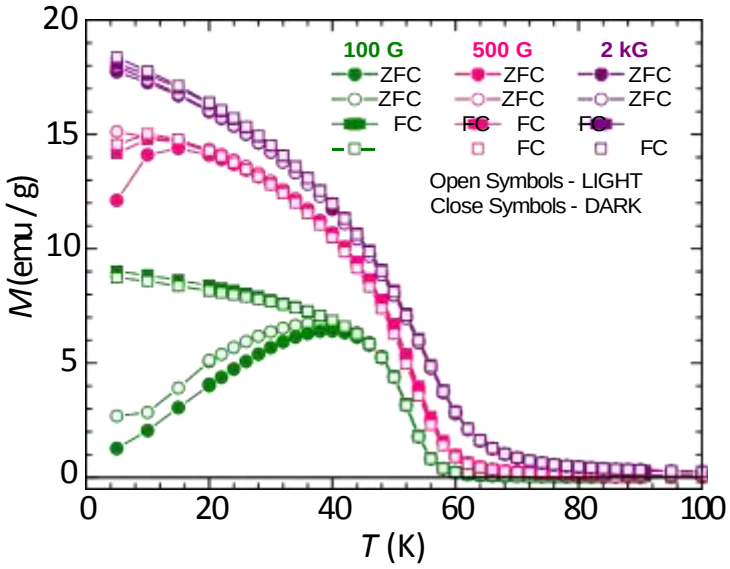

Figure SI-11. The zero-field-cooled (circles) and field-cooled (squares) magnetic profiles of sample **2** in the dark (closed symbols) and light (open symbols) states collected at various applied magnetic fields, contrasting the photomagnetic changes observed at low (100 G) and higher (500 G, 2 kG) applied fields. During field-cooling, an applied field of 100 G was used in all cases. The increasing magnetization with decreasing temperature for the FC magnetization implies the magnetic anisotropy field is greater than the maximum field.

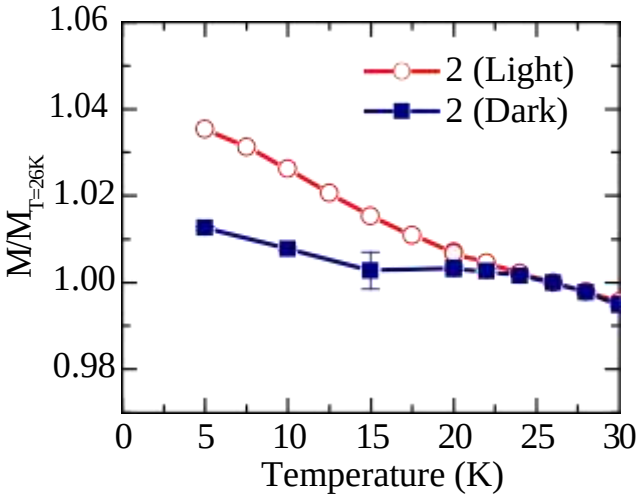

Figure SI-12. SQUID magnetometry data of **2** before and after irradiation normalized to the magnetization value at T = 26 K. These data illustrate the relative magnitudes of the increase in magnetization below 20 K due to Fe-Cr interactions at the interface of the heterostructure particles. Upon irradiation, the LIESST event in the Hofmann component increases the number of HS Fe^{2+} centers, resulting in additional Fe-Cr interactions depicted by an increased magnetization from the dark-state.

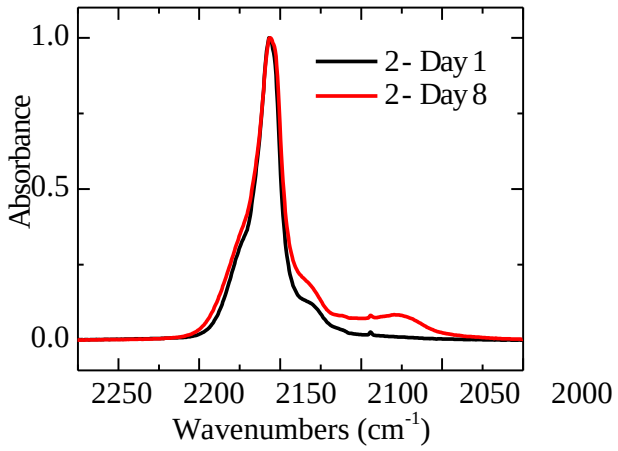

Figure SI-13. Normalized room temperature FTIR spectra in the ν(CN) region of **2** collected immediately after synthesis (black) and several days after synthesis (red). Over time, a mode below 2100 cm^{-1} appears, attributed to linkage isomerism of bridging CN groups at the heterostructure interface. The rearrangement from Fe-NC-Cr to Fe-CN-Cr bridging modes results in much lower vibrational frequencies (~2075 cm^{-1}).

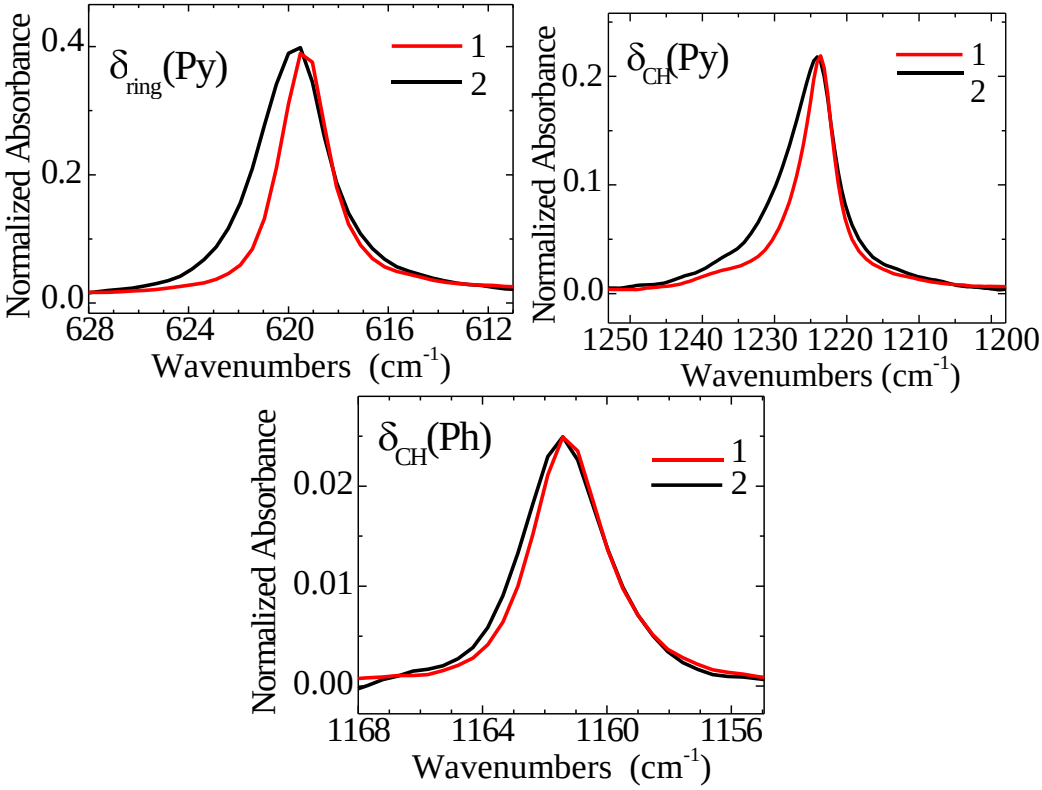

Figure SI-14. Comparison of peak widths in select normalized Hofmann and heterostructure ligand modes, illustrating peak broadening after the heterostructure is formed. Select modes associated with the pyridine (py) and phenyl (ph) rings of the phenylpyridine ligand indicate that some modes are more strongly influenced by heterostructure formation than others. Specifically, the pyridine-related modes appear more closely coupled to the Fe coordination environment than the phenyl-related modes, based on relative extent of asymmetric peak broadening. Vibrational modes were assigned from literature calculations of the phenylpyridine molecule.[44]